Interfacial spin structures in Pt/Tb$_3$Fe$_5$O$_{12}$ bilayer films on Gd$_3$Ga$_5$O$_{12}$ substrates

Roshni Yadav[1], Abdulhakim Bake,[2] Wai Tung Lee,[3] Yu-Kuai Liu[4,5] David R. G. Mitchell[6] Xin-Ren Yang,[1]
David L. Cortie,[2,3,*] Ko-Wei Lin[1,†] and Chi Wah Leung[4,‡]

[1]*Department of Materials Science and Engineering, National Chung Hsing University, Taichung 402, Taiwan*
[2]*The Institute for Superconducting and Electronic Materials, University of Wollongong, Wollongong, New South Wales 2522, Australia*
[3]*Australian Nuclear Science and Technology Organisation, Lucas Heights, New South Wales 2234, Australia*
[4]*Department of Applied Physics, The Hong Kong Polytechnic University, Hung Hom, Hong Kong, China*
[5]*College of Electronic Information and Mechatronic Engineering, Zhaoqing University, Zhaoqing Road, Duanzhou District,
Zhaoqing 526061, Guangdong, China*
[6]*Electron Microscopy Centre, AIIM Building, Innovation Campus, University of Wollongong, Wollongong, New South Wales 2519, Australia*

In this study, we investigate the properties of ferrimagnetic Tb$_3$Fe$_5$O$_{12}$ (TbIG) thin films grown on Gd$_3$Ga$_5$O$_{12}$ (GGG) substrates using the pulsed laser deposition technique. Some of the films are capped with a thin platinum (Pt) layer. We observe a strong temperature-dependent anomalous Hall effect in the films, with sign reversals at the ferrimagnetic compensation temperature ($\sim$240 K) and lower temperatures. X-ray diffraction and scanning transmission electron microscopy (STEM) confirm the high crystalline quality and smooth surfaces of the films, while the Pt layer is found to be polycrystalline. Polarized neutron reflectometry reveals a weak magnetic moment confined to the TbIG layer, and an interfacial magnetic layer at the substrate-film boundary appears at low temperatures (below 10 K). This observation is supported by STEM-energy dispersive x-ray mapping, which indicates a chemical difference in the ratio of Gd:Ga at the TbIG/GGG interface. Unlike YIG/GGG interfaces, the TbIG/GGG interface does not exhibit magnetic dead layers. Additionally, a small, induced magnetization is detected in the Pt heavy metal layer at low temperature, with ferromagnetic coupling to the garnet, potentially influencing the anomalous Hall effect.

I. INTRODUCTION

Recently, there has been a strong interest in ferrimagnet insulator (FI) materials for studying spin Hall magnetotransport effects based on the FI/heavy metal (HM) bilayer structures [1–3]. So far, most studies have focused on yttrium iron garnet (YIG) due to its low damping constant and relatively simple magnetic structure [4]. However, the rare-earth (RE) iron garnet (IG) family can demonstrate complex magnetic structures and their impact on spin Hall related behavior is of great interest. For example, by replacing the *c*-site Y^{3+} with RE^{3+}, the spontaneous magnetization reaches zero at the compensation temperature (T_{comp}) due to the cancellation of the RE^{3+} and the Fe^{3+} sublattice magnetizations [5].

This family of heterostructures shows three significant magnetotransport effects, which are useful for their proposed spintronic applications. Firstly, the temperature dependence of the sublattice moments in the REIG films influences the anomalous Hall resistance (AHR) in the adjacent HM layer [6]. Secondly, a new dynamic magnetoresistance phenomenon known as spin Hall magnetoresistance (SMR) [7] has been identified in these types of structures and is linked

to the spin Hall effect (SHE) and inverse spin Hall effect (ISHE), and this is strongly influenced by the RE component. For example, studies in gadolinium-iron garnet (GdIG)/Pt heterostructures demonstrate that the amplitude of SMR shows significant change around the T_{comp}. of GdIG due to the noncollinear submagnetic moment rotation of GdIG [8,9]. Whereas the anomalous Hall effect (AHE)/SMR studies in Pt/TbIG/GGG films revealed a sign change at T_{comp}., the spin mixing conductance of several Pt/rare-earth garnets shows little reliance on the rare-earth iron [10,11], implying that Fe sublattices dominate spin transport across the HM/magnetic-insulator interface. Thirdly, due to the magnetostrictive effects, some REIG systems can demonstrate perpendicular magnetic anisotropy (PMA) [6,12], the effect of which can be revealed in AHR measurements of REIG/HM bilayers [13,14].

The origin of the useful spin effects described above is broadly attributed to some form of magnetic proximity effect (MPE), as these do not occur for single REIG layers, and only appear in heterostructures with HM/REIG interfaces. It has been argued that magnetic proximity effects (MPEs) between the REIG and the HM provide the mechanism of the SMR and the AHE [15]. The most well-known form of MPE is where a thin interfacial region in the nonmagnetic metal exhibits an induced moment through exchange with the magnetic layer. However, there are closely related effects, such as interface-induced spin anisotropy and dynamic MPE, which

---

*Corresponding author: dcr@ansto.gov.au
†Corresponding author: kwlin@dragon.nchu.edu.tw
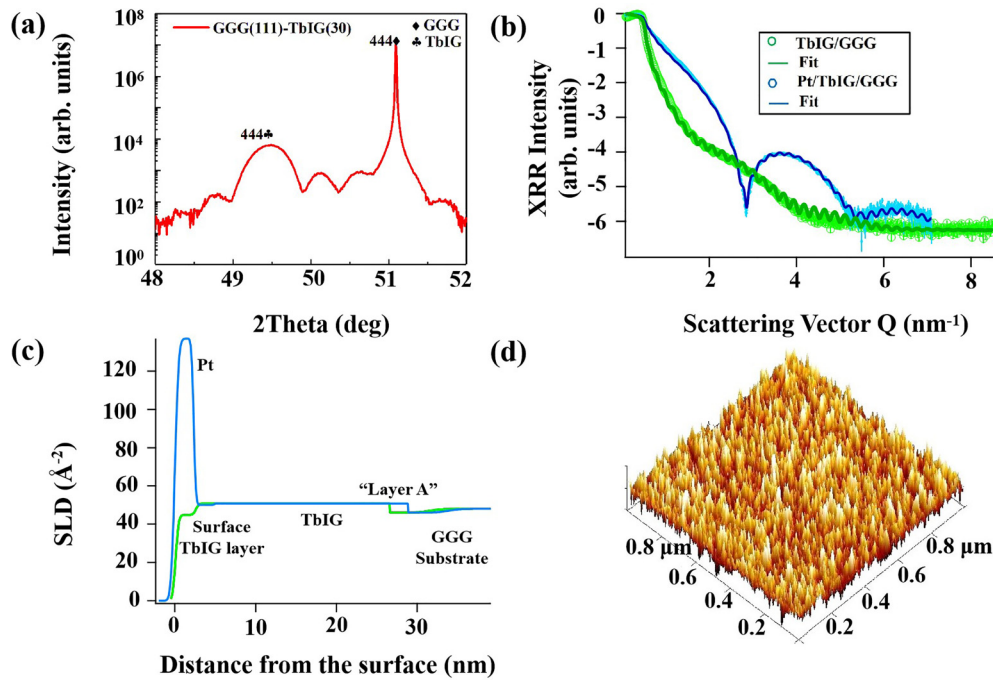‡Corresponding author: dennis.leung@polyu.edu.hk

FIG. 1. (a) High-resolution XRD scan of a TbIG/GGG thin film around the (444) Bragg reflections. (b) X-ray reflectivity of a TbIG/GGG thin film with and without a Pt surface layer. (c) Scattering length density profiles determined from the x-ray reflectometry fits with and without a Pt surface layer. (d) The AFM micrograph of a TbIG/GGG thin film over a 1×1 μm area.

can also be considered proximity effects, although these do not necessarily lead to a locally modified magnetization magnitude [16]. MPE-induced magnetism contributes to the HM's magnetoresistance and couples to the ferromagnet's magnetic moment, making the MPE an essential element in defining the behavior of HM/magnetic heterostructures, especially at low temperatures where the MPE is stronger. However, the lack of mobile electrons in the insulating oxide in HM/magnetic-insulator bilayers indicates that the MPE has a different origin from metallic multilayers, and this is attributed to a superexchangelike interaction with magnetic cations near the surface.

Amamou *et al.* [17] observed the magnetic proximity effect in Pt/CoFe$_2$O$_4$, concluding that Pt induces proximity effects via interactions with Fe ions near the surface. Lu *et al.* [18] reported a measurable MPE in Pt/YIG at 300 and 80 K. However, at 300 K, Geprägs *et al.* [19] found no induced moment in Pt/YIG. Jakubisova *et al.* [20] observed a transition layer at the YIG/GGG interface. Similarly, Mitra *et al.* [21] observed an additional magnetic layer (substrate-YIG interface) in the YIG/GGG thin film at low temperatures ($\leqslant 150$ K). Most recently, Roos *et al.* [22], observed the interfacial layer of (Gd-Y)IG under extremely high magnetic fields at low temperatures (<100 K). The quality of the interface and the growth method are the two factors influencing the MPE. The SMR observed in Pt/YIG [1] arises from the interchange between spin accumulation at the normal metals (NM)/FI interface and the magnetization of the FI layer. However, the relative importance of statically and dynamically induced magnet components in the proximity effect is still the subject of research. In this regard, the role of the interfaces needs to be investigated, and depth-resolved measurements are needed to reveal the changes in the spin structures and the transport behavior in the REIG/HM thin films and their interface. To

this end, we present a detailed study of TbIG/Pt thin films using x-ray, neutron, and electron techniques to resolve the chemical and magnetic structure.

II. METHODS

Ferrimagnetic-insulator Tb$_3$Fe$_5$O$_{12}$ (TbIG) thin films (30 nm) were grown on a (111) oriented Gd$_3$Ga$_5$O$_{12}$ (GGG) substrate [10] (size: 10×10 mm^2) by using the pulsed laser deposition technique (PLD), followed by *ex situ* deposition of Pt with a nominal thickness of 3 nm by rf magnetron sputtering. Details of film deposition and characterization can be found elsewhere [13].

X-ray diffraction (XRD) and reflectometry (XRR) were performed on a Panalytical X'Pert Pro system using Cu $K\alpha$ radiation ($\lambda = 1.54$Å), and data were processed and fitted using the REFNX software package [18].

A field-emission scanning electron microscope (FESEM) (FEI NanoLab G3 CX) coupled with a focused ion beam (FIB) was used to prepare a lamella from the cross section of the Tb$_3$Fe$_5$O$_{12}$ (TbIG) thin films grown on a Gd$_3$Ga$_5$O$_{12}$ (GGG) substrate using the simplified form of the method described previously [19]. Scanning transmission electron microscopy (STEM) (JEOL ARM-200F) was used to characterize the microstructure of the thin films at the atomic scale. The elemental mapping of the thin film's cross section was accomplished using energy-dispersive x-ray spectroscopy (EDX) attached to the STEM. A DI Veeco/NanoMan D3100CL atomic force microscope (AFM) was also used to estimate the thin film's surface topography.

A commercial ULVAC-PHI PHI 5000 Versa Probe x-ray photoemission spectroscope (XPS) was used to determine the oxidation states of the Pt/TbIG/GGG thin films [23].
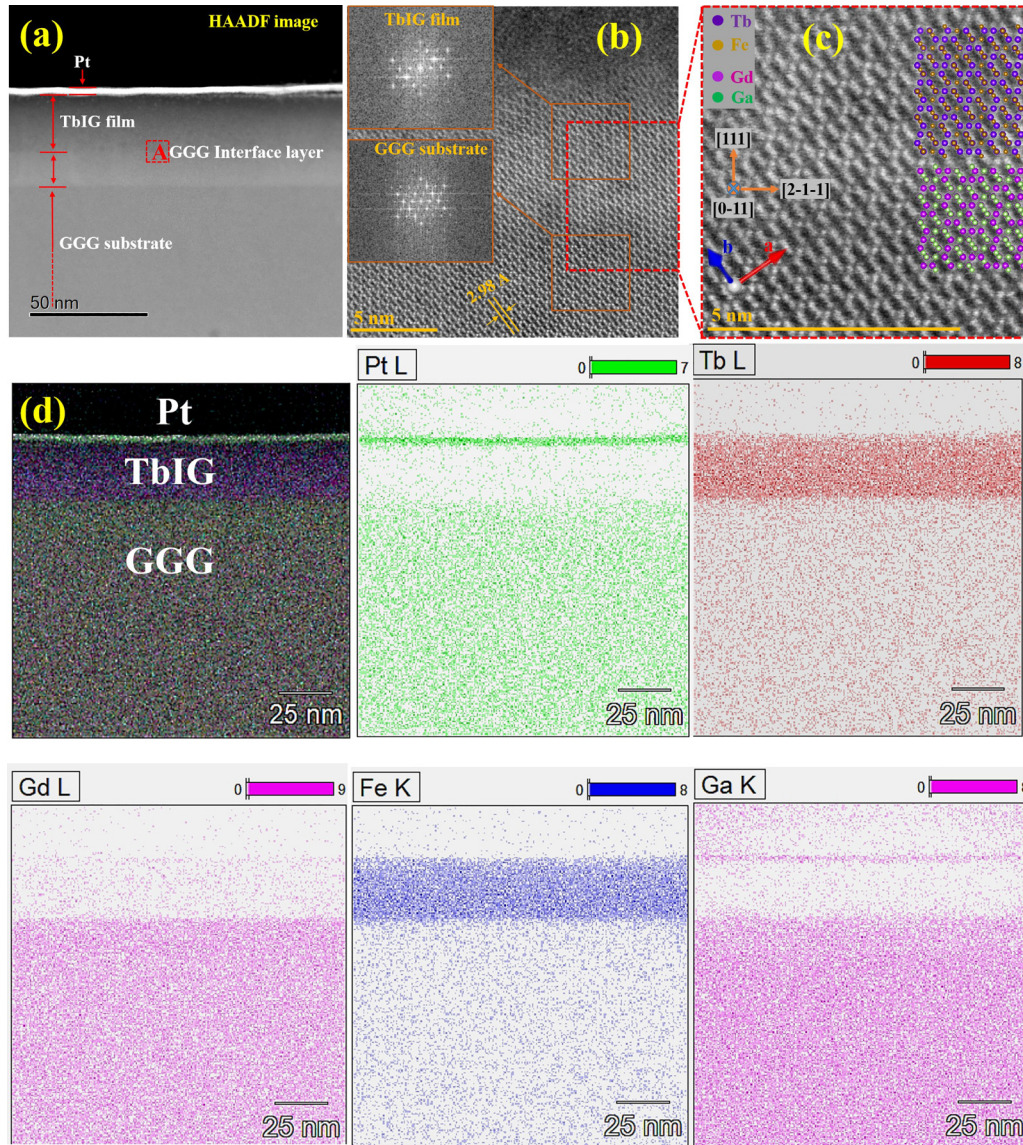
FIG. 2. (a) The cross-sectional HRSTEM (HAADF) image of crystalline TbIG thin film grown on a GGG substrate. The corresponding high-resolution image of box A in (a) is shown in (b). The insets are diffractograms of the boxed regions from the GGG substrate and TbIG film. (c) The enlarged area of (b) with the crystal structures of the TbIG and GGG superimposed. (d) The EDX maps of Pt, Tb, Gd, Fe, and Ga.

Polarized neutron reflectometry (PNR) was conducted using the PLATYPUS reflectometer at the Australian Nuclear Science and Technology Organisation (ANSTO). PNR is an ideal tool for studying magnetic thin films, surfaces, and multilayers by measuring the depth profiles of magnetic moment distributions in thin films or multilayers from the surface to the substrate [24]. Here PNR was used to study the spin structure of TbIG with a nominal thickness of 30 nm above, below, and near the compensation temperature ($T_{\text{comp}} = 243$ K) [13]. PLATYPUS is a time-of-flight instrument that uses neutrons with wavelengths ranging from 2.8 to 12.5 Å (when polarized) [24]. The spinning mechanical choppers can be adjusted to achieve variable wavelength resolution. In this work, a combination of two choppers (labeled "1" and "3" on the instrument) operating at 33 Hz was chosen, yielding a theoretical wavelength resolution of d$\lambda/\lambda = 3.5\%$. A four-slit system

was used to collimate the beam and provide a matching angular resolution. The full details of the slit/instrument settings are included in the experimental metadata in the Supplemental Material [25]. A Fe/Si supermirror with $\sim$99.3% polarization was used to polarize the beam. The reflection pattern is plotted as a function of the out-of-plane scattering vector, $Q_z = 4\pi \sin\theta/\lambda$, where θ is the scattering angle as stated in standard Bragg-Brentano geometry [26]. The reflection of the two neutron spin states (R_{++} and R_-) shows a strong dependency on Q. The subscripts "++" and "−" denote whether the neutron spin is parallel or antiparallel to the applied magnetic field for the incident (first subscript) and reflected beams, respectively (second subscript). The spin asymmetry (SA) often denoted as SA = $(R_{++}\text{-}R_-)/(R_{++} + R_-)$, is a measure of the magnitude of the magnetization component that aligns either parallel or antiparallel to both the neutron spin and
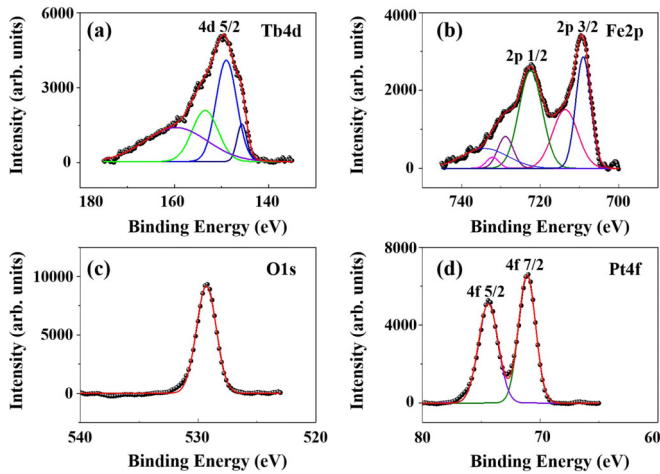
FIG. 3. The XPS spectrum of (a) Tb $4d$, (b) Fe $2p$, (c) O $1s$, and (d) Pt $4f$ as measured in a TbIG film for Pt/TbIG/GGG thin films.

the external magnetic field, with its magnitude being directly proportional to the difference between the R_{++} and $R_{-}-$ reflectivity [27].

The PNR data were fitted with the SIMULREFLEC software [28], and the thin-film thickness measured from STEM images was used to constrain the fitting model. Complementary fitting and Monte Carlo Markov chain (MCMC) sampling were performed using the REFNX software [29] package to reveal the details of the magnetic interfaces and the associated uncertainties. The reduction and fitting scripts are attached in the Supplemental Material as Jupyter Notebooks [25].

III. RESULTS AND DISCUSSIONS

X-ray diffraction and reflectometry techniques were used to measure the average long-range structure of the thin films. Figure 1 shows the XRD and XRR patterns obtained for the TbIG/GGG films. Only the (444) Bragg reflections are visible for the substrate and film in the XRD, as shown in Fig. 1(a), indicating a single crystalline film that matches the orientation of the underlying substrate. The d spacing for the GGG (444) substrate is 1.785 Å, and the TbIG (444) is 1.795 Å. The lattice parameter of GGG is 12.35 Å and the TbIG is 12.42 Å. Both agree with reported values in the International Inorganic Crystal Structure Database (ICSD) for cubic garnet forms (#ICSD192181 and #ICSD 9233). The observed compressive stress of a TbIG film grown on a GGG substrate is 0.56%. Figure 1(b) shows an XRR scan of the TbIG film and the Pt/TbIG bilayer on GGG (111). The TbIG and the GGG substrate have very similar electron density, which determines their x-ray scattering length density (SLD) (a measure of x-ray refractive index). This explains the relatively featureless reflectometry pattern for the uncoated TbIG/GGG films, as the lack of contrast reduces the amplitude of the high-frequency fringes. In contrast, the sharp reflectometry Kiessig fringes in the x-ray reflectometry for the film with the Pt layer indicate a sharp Pt/TbIG interface with substantial modifications caused by the large difference in electron density of the heavy metal and the oxide. Fits to the data were used to obtain the SLD profile shown in Fig. 1(c). From these fits, the Pt layer has a

thickness of 2.4 ± 0.5 nm. In contrast, the overall thickness of the TbIG layer cannot be reliably determined because there is insufficient contrast between the TbIG and GGG. However, for self-consistency, the values from the cross-sectional STEM and PNR (see later sections) were used to constrain the fit, including the presence of the additional interface at the TbIG/GGG interface labeled "A" (as described in a later section discussing the STEM). From the SLD profiles, both layers' surface and interface roughness are below 5.0 Å. This is confirmed by complementary atomic force microscopy (AFM), performed over a scan area of 1 µm × 1 µm shown in Fig. 1(d). The AFM image appears uniform and smooth, and the surface roughness of the TbIG thin film is 2.0 Å (root-mean squared).

High-resolution cross-sectional STEM was conducted to provide complementary atomic-scale insight into the structure (Fig. 2). The cross-sectional high-angle annular dark field (HAADF) image for the overall film structure is shown in Fig. 2(a). The topmost layer, which appears bright in the image, is the thin Pt layer with a thickness of 2.3 nm, consistent with the earlier XRR results. Underneath the metallic layer, the first layer is the TbIG film with a thickness of 24.5 nm (compatible with the neutron reflectometry data later). The second layer, marked A, is a layer with modified stoichiometry at the top of the GGG substrate, and the bottom region is the infinite GGG substrate. It is difficult to directly measure the thickness of layer A from the STEM due to the low contrast with a gradient composition, but it is estimated to have a thickness of ∼6-14 nm. In the HAADF image, the contrast varies as an approximate function of the mean atomic number (Z^2) of the phase [30] and, as such, the Tb and Gd garnets have similar brightness. The enlarged high-resolution HAADF image (box A) is illustrated in Fig. 2(b), showing essentially the same atomic structure in each layer, consistent with high-quality epitaxial growth that provides a single crystalline heterostructure. Although there is some variation in the Gd, Ga, and Tb ratios in the structure, as shown later by the EDX, the crystal structure overall is the same throughout the oxide region, where the garnet structure is preserved, with no apparent interfacial defects or dislocations. The inset of Fig. 2(b) shows the fast Fourier transform (FFT) diffractograms of the substrate and films. The identical sets of spots in the FFT diffractogram for the TbIG and GGG regions show that the layers are coherent and have the same orientation and structure. This is consistent with the [0- [11]] crystal axis projection, with the [111] axis vertical, as expected, shown in the superposition of the enlarged region in Fig. 2(c). The HRSTEM results, therefore, agree well with the XRD and XRR results.

The heavier atoms of Gd in the thin film shown in Fig. 2(c) are represented by brighter spots, which match extremely well with the overlay of purple dots representing heavier atoms of Gd in GGG and blue dots representing Tb plotted by the VESTA crystallographic software [31]. Thus, the TbIG film was epitaxially formed on the GGG substrate, according to the HRSTEM results. Figure 2(d) shows element mapping images using EDX, revealing a nearly homogeneous composition distribution in each layer and no obvious intermixing at the TbIG/GGG interface. Close inspection of the boxed region labeled "A" in Fig. 2(a), however, showed that the Ga:Gd ratio
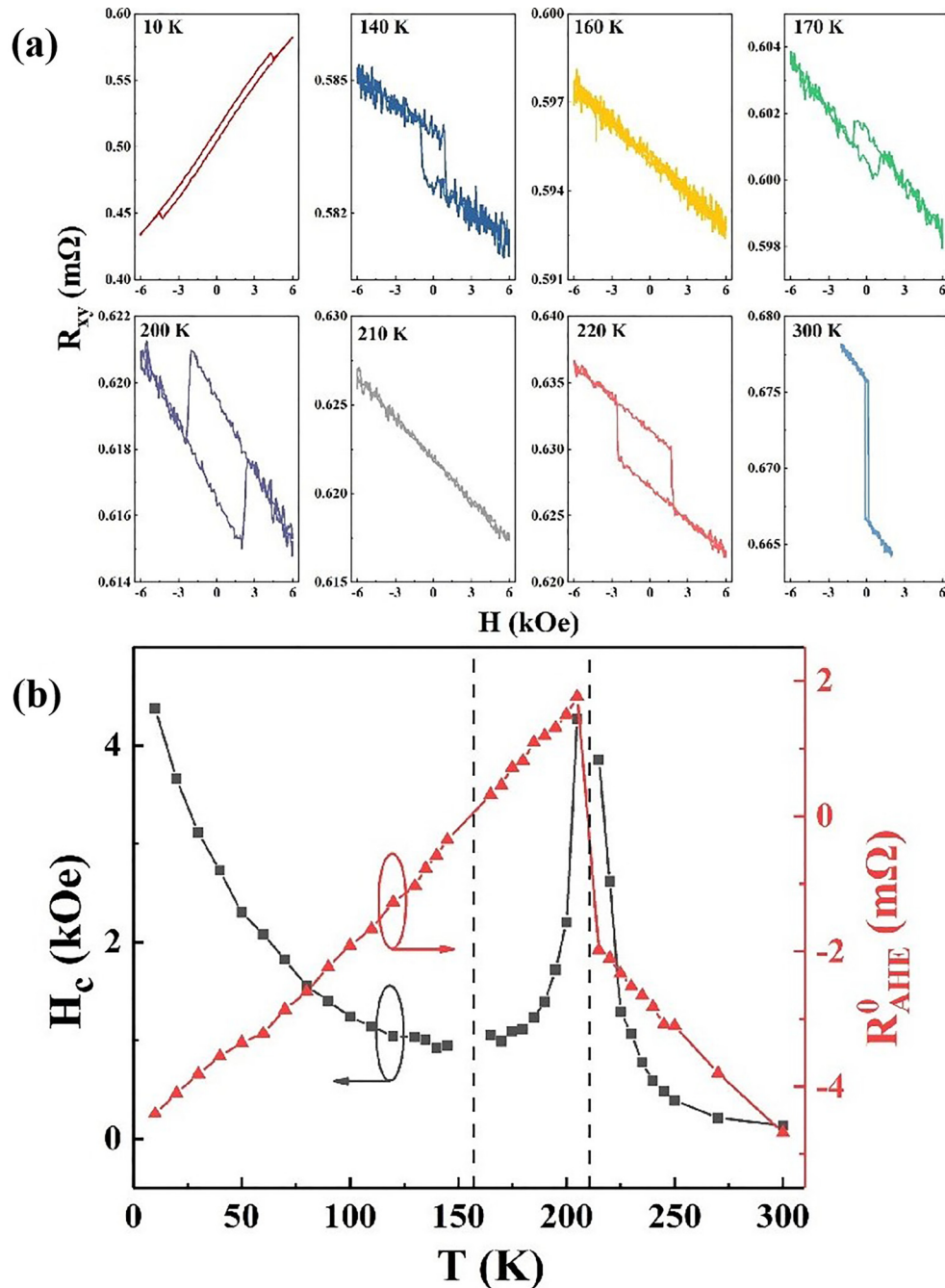
FIG. 4. Temperature-dependent $R_{xy}-H$ loops of a Pt/TbIG bilayer. (a) R_{xy} as a function of the out-of-plane magnetism between 10 and 300 K. Note that the y-axis scale is different among these plots to highlight the variation of the plot shapes and R_{AHE} signs with changing temperatures, where R_{AHE} is obtained after removing the linear background of R_{xy}. (b) Temperature dependence of R_{AHE}^0. (c) The temperature dependency of H_c from $R_{AHE}-H$ loops.

of the interface differed from the primary GGG substrate. Thus this layer is a Gd:Ga garnet structure with modified stoichiometry rather than an interdiffusion layer. We note that the weak signal of the Ga in the Pt layer is a byproduct of the STEM sample preparation process which uses a Ga-focused ion beam as a tool to prepare electron-transparent cross sections.

X-ray photoelectron spectroscopy (XPS) was used to analyze the oxidation state in the Pt/TbIG/GGG thin film. The XPS spectrum for Tb $4d$ positioned at 149.5 eV stipulates

the presence of Tb^{3+} in the TbIG film [Fig. 3(a)] as also observed by Gnanasekar *et al.* [32], which is comparable to the bulk state of Tb $4d$ 5/2 (i.e., 149.9 eV) [32]. The Fe$2p$ XPS spectrum of the Pt/TbIG/GGG thin film is shown in Fig. 3(b). The deconvoluted Fe $2p$ peak shows the doublet Fe $2p_{3/2}$, and Fe $2p_{1/2}$ peaks positioned at 709.5 eV (Fe^{3+}) and 722.3 eV (Fe^{2+}). This shows that the iron in the thin film exists in both the Fe^{2+} and Fe^{3+} states as observed in Fig. 3(b), which is the same as in the bulk state [i.e., 709.4 eV (Fe $2p_{3/2}$) and 722.2 eV (Fe $2p_{1/2}$)] [33]. Figure 3(c) shows an O $1s$ spectrum with
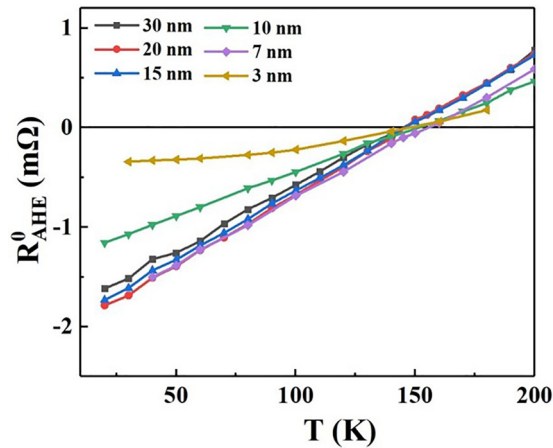
FIG. 5. R_{AHE}^{0} extracted from temperature-dependent R-H loops of Pt/TbIG bilayers with the garnet thicknesses ranging from 3 to 30 nm [36].

FIG. 7. Pt/TbIG/GGG: PNR data sets (dots) and best fits (solid lines) at 7 K under a 1 T in-plane field. (a) The reflectometry curves and (b) spin asymmetry.

a peak at a binding energy of 529.2 eV, indicating the O^{2-} ion in the lattice as O 1s metal oxide comparable to its bulk value, i.e., 529.5 eV [34]. The Pt 4f peaks [Fig. 3(d)] are observed at 71.3 and 74.6 eV, which is comparable to its bulk value, i.e., 71.34 and 74.65 eV, respectively, corresponding to the binding energies of the Pt 4$f_{7/2}$ and Pt 4$f_{5/2}$ which represents the Pt^{0} state i.e., zero-valent state [35].

To explore the anomalous Hall effect (AHE) in similar Pt/TbIG bilayers processed into Hall bar devices, Fig. 4(a) shows the field-dependent Hall resistance (R_{xy}−H) loops as a function of temperature. The AHE signal can be obtained after subtracting the linear background of the plots. All of the R_{xy} loops exhibit hysteresis behavior. However, the sign of the AHE coefficient is highly dependent on the temperature. R_{AHE} is negative at lower temperatures ($T < 160$ K). When the temperature is slightly above 160 K, a change in the sign of R_{AHE} is observed. The magnitude of R_{AHE} continues to rise as the temperature increases to 210 K. At roughly 210 K, R_{AHE} undergoes another sign reversal that persists until room temperature (300 K), i.e., R_{AHE} retains its opposing sign, but its amplitude decreases as temperature rises. The variation of R_{AHE} at zero fields (R_{AHE}^{0}) as a function of temperature is extracted from Fig. 4(a) and is plotted in Fig. 4(b). The
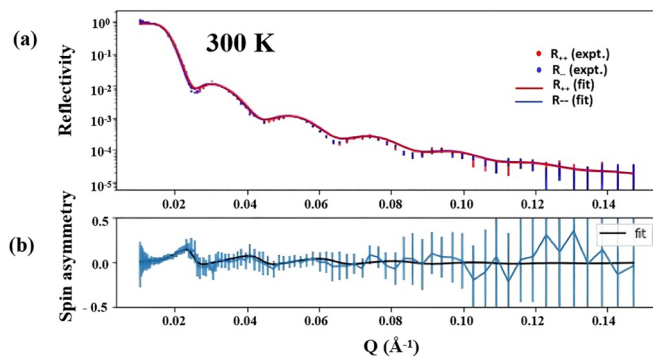

FIG. 6. Pt/TbIG/GGG: PNR data sets (dots) and best fits (solid lines) at 300 K under a 1 T in-plane field. (a) The reflectometry curves and (b) spin asymmetry.
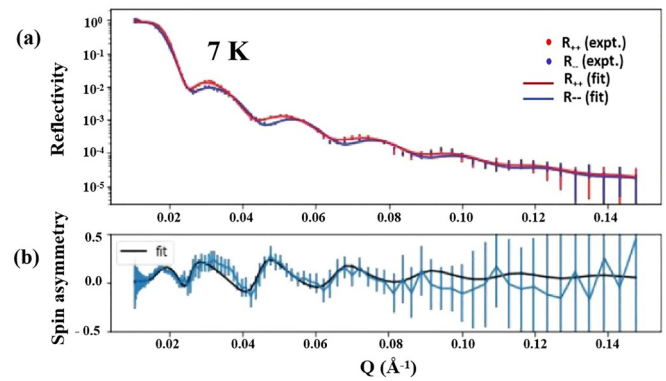
H_c of the TbIG, as measured by R_{AHE} is the bulk property of the TbIG film. Given the good stability of TbIG, a H_c similar to the current work and that of Ref. [13] was found. Similar results have been reported by Shao *et al.* [14]: the cross-over at low temperature is a competition between the magnetic proximity effect and the intrinsic magnetization of the garnet, while the higher-temperature crossover coexists with the compensation temperature of TbIG. The latter observation is supported by the coercivity (H_c) vs temperature plot [Fig. 4(b)], which shows the divergence about T_{comp}. In the current study, we deposited the Pt electrode directly after the TbIG film was removed from the chamber, as we have found this leads to greater reproducibility in the transport data compared to earlier studies which used Pt Hall bars deposited days or weeks after the TbIG growth [13]. Using this method, we consistently find the low-temperature cross-over in R_{AHE}^{0} at 150 – 160 K (Fig. 5), independent of film thickness, as also discussed in more detail in our recent work [36].

To clarify the chemical and magnetic depth profile in the continuous Pt/TbIG/GGG films, and the magnetic role of the heavy metal in the complex anomalous Hall behavior, PNR was conducted to yield nm-scale resolution on the magnetism in each of the distinct layers. Figure 6(a) shows the polarized neutron reflectivity at 300 K at a magnetic field of 1 T for the Pt-capped TbIG. As the TbIG and Pt both have low magnetization (<200 emu/cm^3), the distinctions between spin-up R_{++} and spin-down R₋ reflectometry profiles are subtle. However, these are far more apparent at low temperature (7 K) [Fig. 7(a)] than at room temperature (300 K) [Fig. 6(a)]. To enhance the visibility of magnetic differences, the bottom section of the plots shows the SA calculated at 300 K [Fig. 6(b)] and 7 K [Fig. 7(b)] from the differences of R_{++} and R₋, highlighting the detectable changes in the magnetic contribution to the neutron refractive index (SLD). The 300 K data show a small amount of SA, indicating a weak in-plane magnetization as expected for the ferrimagnetic oxide (TbIG). This is modeled by including a small magnetic component to the SLD in the fits described in the next section. A large magnetization in the thin film is evident at the lower temperature (7 K) from the apparent splitting between the spin-up (R_{++}) and spin-down (R₋) reflectivity. Both the shifted peak position of the SA and the additional oscillations in the 7 K SA data
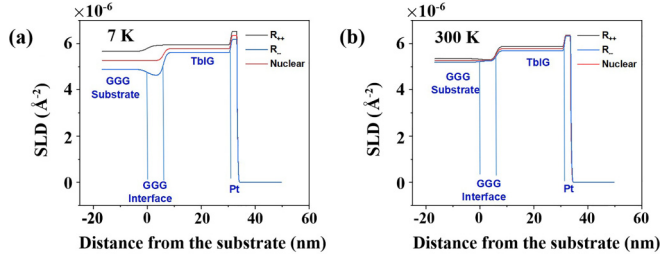
FIG. 8. Pt/TbIG/GGG: Scattering length density (SLD) at (a) 7 K and (b) 300 K.

indicate the magnetic depth profile is different from the 300 K data. The solid points are the data, and the solid lines are fits using the model described below.

A four-layer model was used for fitting the 7 and 300 K data, respectively, both measured under a 1 T in-plane field. The four layers account for the Pt layer, TbIG layer, GGG interface region, and the GGG substrate. Figures 6 and 7 show the data of neutron reflectivity and SA and their fits. From the fit, the thickness of the TbIG layer is ∼25 nm. The thickness of the Pt film could not be accurately determined from the PNR alone, since it has a negligible effect on the PNR reflectivity owing to the narrow available Q range. However, it was constrained to be 2.4 nm to be consistent with the STEM and XRR. The main advantage of the PNR fits is that they yield unique insights into the magnetic profile which is not detectable using STEM or XRR. The PNR data were fitted to a SLD profile to quantify the layer magnetization and the results are shown in Fig. 8. The PNR fit shows that at 300 K the magnetization is only detected in the TbIG layer, with a weak overall contribution. In contrast, for the 7 K data, detailed fitting of the neutron SA shows that the overall magnetization is much larger. Furthermore, to fit the complex Q dependency, it is clear that this cannot be described by a model where the magnetization solely arises from the TbIG layer. Instead, a more significant portion of the additional magnetization originates from the GGG interfacial region. A small portion of the magnetization also arises from an induced magnetic layer in the Pt film. There is considerable uncertainty for the small Pt magnetization, as discussed later. The best-fit parameters are shown in Table I, and later, an analysis of the uncertainty in the parameters is given using Monte Carlo sampling [37,38]. To facilitate comparison with magnetometry, we have also

converted the magnetic SLD value into a magnetization using the standard coefficient relating the magnetic SLD and volume magnetization: $C' = 2.91 \times 10^{-9}\,\text{Å}^{-2}\text{cm}^3/\text{emu}$ [39].

The peak values of the net SA for different temperatures for comparison are summarized in Table II. The key point is that the SA [Fig. 6(b)] above 100 K is very small; however, below 10 K [Fig. 7(b)] there is an additional, strong magnetic component indicating more complex interfacial magnetism is present. The complex magnetism gives rise to the additional peak in the SA that occurs at $Q_z = 0.018\,\text{Å}^{-1}$ for the 7 K temperature. Notably, the Q-dependent oscillations in the SA are damped in the 300 K data, which strongly suggests that an additional layer becomes magnetic at low temperatures, and this is borne out by the fitting. The best fits indicated that the primary source of the low-temperature magnetism is the nonstoichiometric layer (marked A) in Fig. 2. In contrast, the Pt moment is small, making a far lesser contribution. This was confirmed by control measurements on Pt-free TbIG film which also showed the additional SA below 10 K. The measurements, therefore, show that the magnetic structure in TbIG/GGG is complicated by the appearance of a secondary magnetic layer at the TbIG/GGG interface, which appears to arise from a nonstoichiometric section (Ga-rich phase) of the GGG substrate.

From the fits, the SLDs for Pt/TbIG/GGG at 7 and 300 K are shown in Figs. 8(a) and 8(b), where the observed nuclear scattering length density (NSLD) for TbIG is $5.79 \times 10^{-6}\,\text{Å}^{-2}$ and $5.78 \times 10^{-6}\,\text{Å}^{-2}$ at 7 and 300 K. The net magnetic moment in the REIG is contributed to by both Fe^{3+} and Tb^{3+} (TbIG) of the rare-earth (RE) ion. The ferrimagnetic order in REIG is due to the antiferromagnetic interactions in a unit cell between an uneven number of Fe^{3+} ions on the tetrahedral and octahedral sites [5,6]. The SLD at 7 K [Fig. 8(a)] shows a clear splitting between the two profiles related to R_{++} and R_{-}. This indicates a high magnetic moment related to the region present between TbIG/GGG (layer A). This is

TABLE II. Spin asymmetry.

Temperature (K)	Scattering vector Q_z (Å^{-1})	Experimental (arb. units)	Fitting SA (arb. units)	Error bar (arb. units)
300	0.023	0.18	0.11	0.010737
7	0.018	0.14	0.11	0.001746

TABLE I. Four-layer model for PNR fitting of Pt/TbIG/GGG.

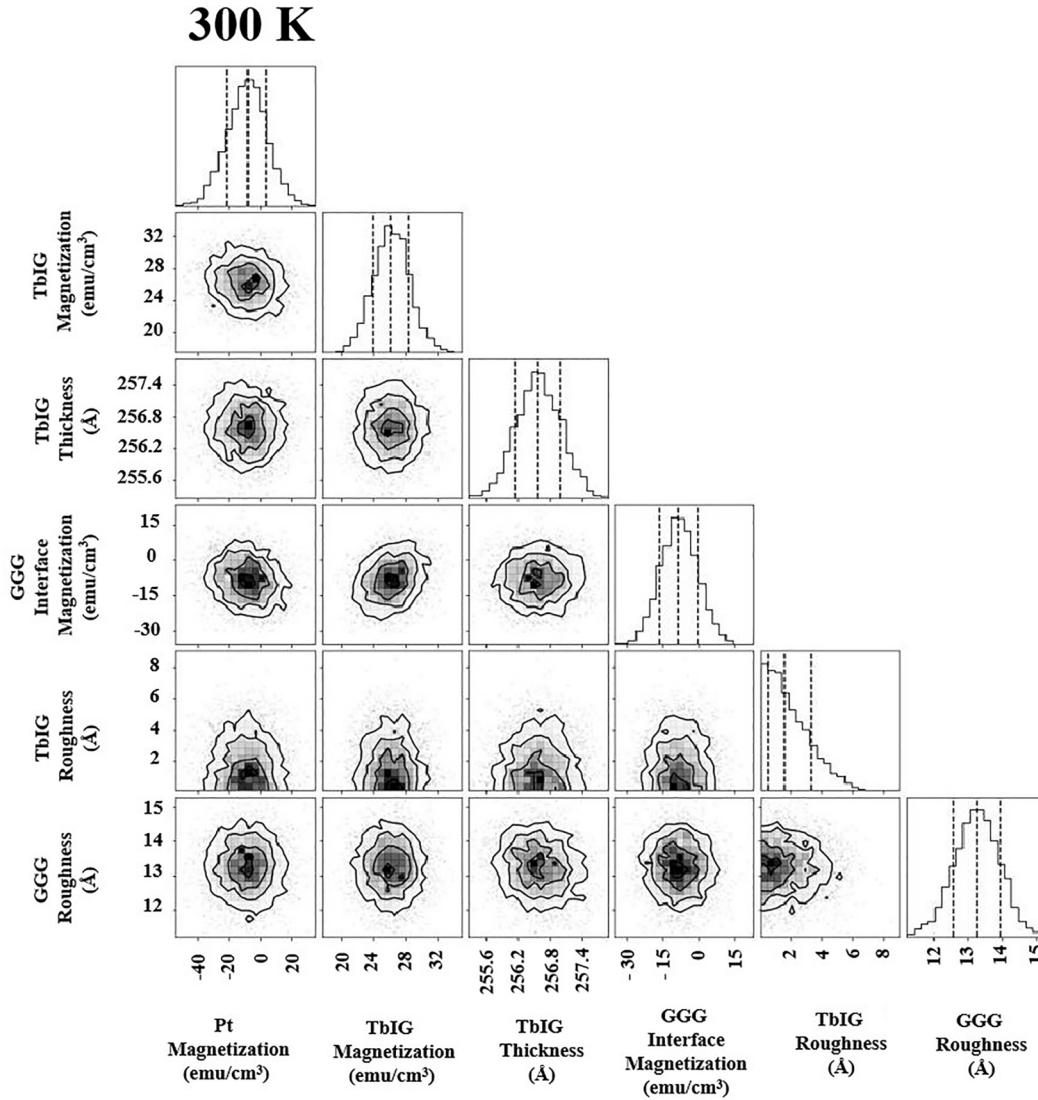| Temperature (K) 300 K	Thickness (nm)	Magnetization (emu/cm^3)	Density (10^{28}/m^3)	Neutron scattering lengths (b/bi) (fm)	Magnetic/structural roughness (nm)
Pt	2.4 (fixed)	6 ± 5	6.62	9.6	0.1 (fixed)
TbIG	25.3 ± 0.1	29 ± 2	0.41	139	0.4 ± 0.2
GGG interface	6 (fixed)	5 ± 4	0.42	125 +41.46i	1.3 ± 0.1
GGG substrate	∞	20 ± 10	0.42	125+41.46i	2.5 (fixed)
7 K					
Pt	2.4 (fixed)	70 ± 12	6.62	9.6	0.1 (fixed)
TbIG	24.9 ± 0.1	55 ± 3	0.41	139	0.8 ± 0.6
GGG interface	6 (fixed)	208 ± 10	0.42	125+41.46i	1.3 ± 0.1
GGG substrate	∞	117 ± 13	0.42	125+41.46i	2.5 (fixed)

300 K

FIG. 9. The Monte Carlo sampling map shows the correlation and uncertainty between fitting parameters for the neutron reflectometry dataset for Pt/TbIG/GGG at 300 K. The Pt magnetization is vanishingly small at room temperature with the minima centered near 0 emu/cm^3.

in contrast to the SLD at 300 K which shows a small splitting between the two depth profiles indicating only a small magnetic moment in Fig. 8(b). An induced magnetic layer is also observed at the interface of Pt/TbIG at 7 K [Fig. 8(a)]. However, this is a much smaller effect, which can be explained as the induced magnetic dipole moment in Pt caused by the MPE [18]. The MPE becomes prominent due to the interfacial exchange coupling between Pt and the TbIG electrons, which overcomes the thermal fluctuations and gives rise to a magnetic moment induced in the interfacial heavy metal (Pt) layer. Similar effects have been observed in tungsten (W)/TmIG thin films [14] where the PNR results at 200 and 80 K show coupling between W and TmIG with an induced magnetization of similar magnitude ($\sim$50 emu/cm^3); however, in that case the magnetic coupling across the interface was antiferromagnetic (antiparallel). While induced magnetic layers have therefore been reported in other garnets, the present PNR data present a rare observation of a ferromagnetically coupled induced magnetization at Pt/TbIG interfaces.

As the magnetic structure is relatively complex with two distinct "spinterfaces," and the Pt moment is relatively weak, it is worthwhile using advanced fitting methods to assess the correlation and uncertainty in all of the fitting parameters. To this end, the Monte Carlo Markov chain (MCMC) sampling method [38] is a powerful technique to perform Bayesian analysis. The principle is to analyze how the fitting residual (χ^2) varies for sets of parameters sampled randomly in parameter space, computing the log-likelihood, based on the prior and posterior probabilities. The Supplemental Material [25] contains two Jupyter notebooks illustrating how this is implemented in the REFNX software. Figure 9 shows the correlation between the fitting parameters as a corner plot for the 300 K data. Darker regions in the heat map/contour plots correspond to higher probability fits, where the central values are the "best-fit" parameters reported in Table I. Clear minima are noted in most cases, with an isotropic circular distribution implying no correlation between the two varied parameters (which are given by the vertical and
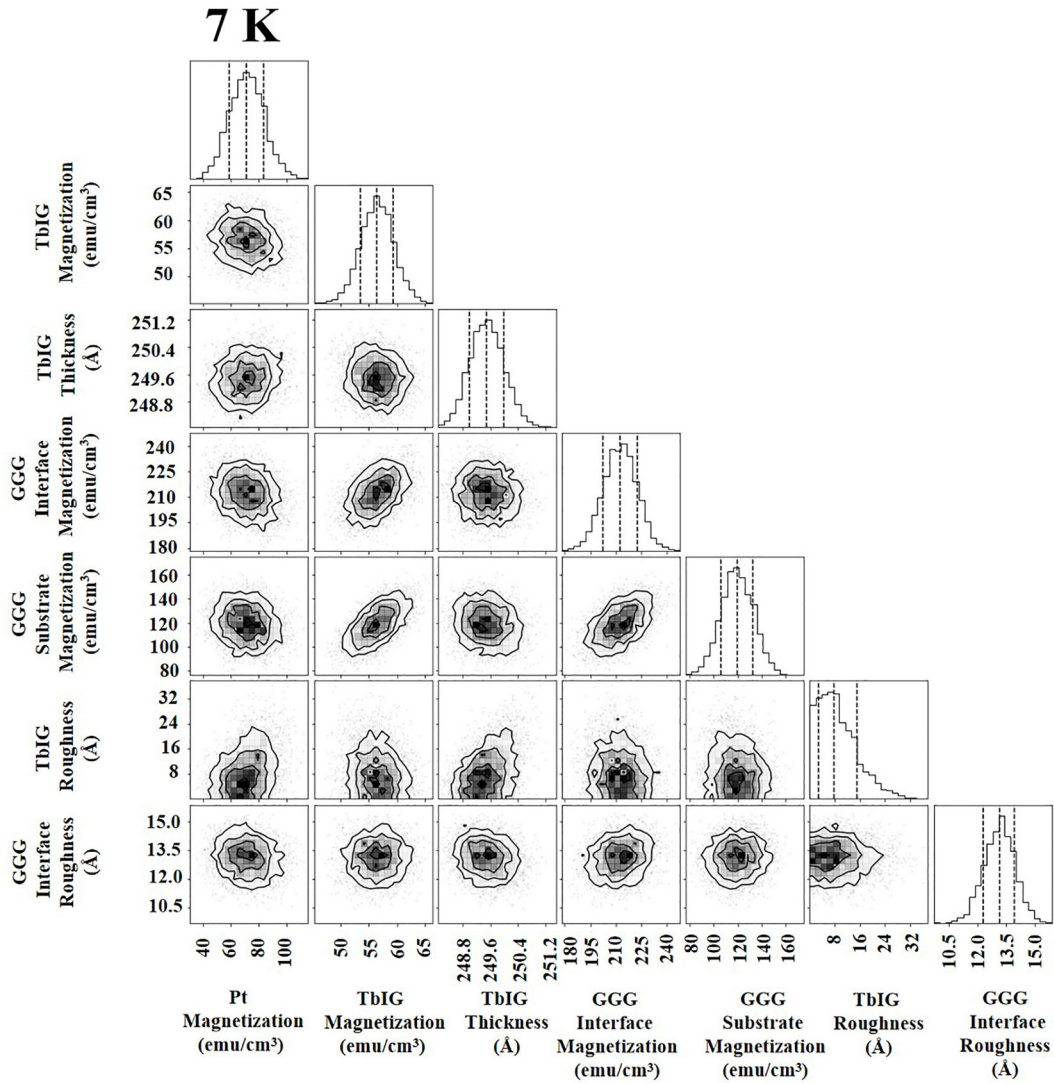
FIG. 10. Monte Carlo sampling map shows the correlation and uncertainty between fitting parameters for the neutron reflectometry dataset for Pt/TbIG/GGG at 7 K. A sizable magnetic moment is detected at the TbIG/GGG interface. At low temperature, the Pt also exhibits a small induced moment, as evident from the minima centered around 70 emu/cm^3.

horizontal axis labels, respectively). In some cases, slightly ellipsoidal distributions are obtained, implying a correlation in the fits (for example, between the TbIG magnetization and the GGG interface magnetization). The histogram plots on the right are used to estimate the uncertainties on each of the parameters, as reported in Table I, using the standard deviation. Most importantly, the magnetization of the Pt layer at 300 K is negligibly small (i.e., 6 ± 5 emu/cm^3). Likewise, the GGG interface [the region labeled "A" in Fig. 2(a)] has negligibly small detectable magnetism (i.e., 5 ± 4 emu/cm^3) at 300 K.

In contrast, Fig. 10 shows a similar statistical analysis performed for the 7 K data. Again, based on the width of the Gaussian in each plot, the uncertainty of the parameters was estimated, and this is included in the error bars in Table I. Most importantly, these results show that at 7 K, a clear induced moment appears in the Pt with a small but detectable magnetization of 70 ± 12 emu/cm^3. We note that this magnetization in the heavy metal is aligned ferromag-

netically with the applied field and TbIG magnetization. The magnitude of the observed magnetization is similar to past PNR studies of heavy-metal tungsten (W) on TmIG where the induced magnetization was 53 emu/cm^3; however, in that case the induced magnetization was antiferromagnetically aligned with the garnet magnetization [14]. In our study, the GGG substrate and GGG interface also have a larger magnetization of 117 ± 13 and 208 ± 10 emu/cm^3 respectively, which were not noted in the past work. However, we have measured at a lower temperature (7 K) than the latter study (80 K/200 K), and the $4f$ magnetization and susceptibility in GGG are expected to be strongly temperature dependent, which explains the different observations.

IV. CONCLUSION

This work shows that it is possible to achieve epitaxial growth of TbIG films on GGG(111) substrates. Although the crystal quality is excellent overall, the chemical structure

of the GGG/TbIG interface is complicated by the presence of a nonstoichiometric Ga-rich phase. This is attributed to the growth conditions during the substrate heating, which warrants further investigation in the future. Intriguingly, the Ga-rich region of the GGG substrate becomes increasingly magnetic at 7 K. Future work is needed to determine if modified Ga:Gd ratios can be used to intrinsically engineer the magnetism of GGG or whether the latter feature is simply a proximity response to a nearby TbIG layer. When the TbIG films are coated by a Pt layer, a strong induced anomalous Hall effect is observed, which reverses in sign at the compensation temperature of the TbIG and reverses again at a lower temperature. This unusual behavior is attributed to the presence of the two magnetic sublattices (Tb) and (Fe) in the garnet, which leads to complicated proximity effects in the Pt layer. Polarized neutron reflectometry reveals an induced ferromagnetically aligned magnetic moment in the Pt at 7 K; however, the moment at 300 K is negligibly small. Despite this, the anomalous Hall effect is certainly detectable at 300 K. This supports the concept that a large, induced moment is not a prerequisite for the anomalous Hall effect in HM/FI heterostructures [1] and, instead, dynamic spin-polarization effects play the dominant role. Nevertheless, the increasing presence of the induced moment at low temperature may introduce secondary effects, which may play a role in the sign inversion of the AHE at low temperature. Our measurements will be valuable in the effort to develop a comprehensive theory to explain the role of electronic effects and induced magnetism on the sign inversion of the AHE. On the phenomenological level, this offers intriguing possibilities for temperature-responsive spintronics.

[1] H. Nakayama, M. Althammer, Y. T. Chen, K. Uchida, Y. Kajiwara, D. Kikuchi, T. Ohtani, S. Geprägs, M. Opel, S. Takahashi, R. Gross, G. E. W. Bauer, S. T. B. Goennenwein, and E. Saitoh, Spin Hall magnetoresistance induced by a nonequilibrium proximity effect, Phys. Rev. Lett. **110**, 206601 (2013).

[2] Y. T. Chen, S. Takahashi, H. Nakayama, M. Althammer, S. T. B. Goennenwein, E. Saitoh, and G. E. W. Bauer, Theory of spin Hall magnetoresistance, Phys. Rev. B **87**, 144411 (2013).

[3] M. Althammer, S. Meyer, H. Nakayama, M. Schreier, S. Altmannshofer, M. Weiler, H. Huebl, S. Geprägs, M. Opel, R. Gross, D. Meier, C. Klewe, T. Kuschel, J. M. Schmalhorst, G. Reiss, L. Shen, A. Gupta, Y. T. Chen, G. E. W. Bauer, E. Saitoh *et al.*, Quantitative study of the spin Hall magnetoresistance in ferromagnetic insulator/normal metal hybrids, Phys. Rev. B **87**, 224401 (2013).

[4] M. C. Onbasli, A. Kehlberger, D. H. Kim, G. Jakob, M. Kläui, A. V. Chumak, B. Hillebrands, and C. A. Ross, Pulsed laser deposition of epitaxial yttrium iron garnet films with low Gilbert damping and bulk-like magnetization, APL Mater. **2**, 106102 (2014).

[5] S. Geller, J. P. Remeika, R. C. Sherwood, H. J. Williams, and G. P. Espinosa, Magnetic study of the heavier rare-earth iron garnets, Phys. Rev. **137**, A1034 (1965).

[6] E. R. Rosenberg, L. Beran, C. O. Avci, C. Zeledon, B. Song, C. Gonzalez-Fuentes, J. Mendil, P. Gambardella, M. Veis, C. Garcia, G. S. D. Beach, and C. A. Ross, Magnetism and spin transport in rare-earth-rich epitaxial terbium and europium iron garnet films, Phys. Rev. Mater. **2**, 094405 (2018).

[7] S. Cho, Sh. Baek, K. D. Lee, Y. Jo, and B. G. Park, Large spin Hall magnetoresistance and its correlation to the spin-orbit torque in W/CoFeB/MgO structures, Sci. Rep. **5**, 14668 (2015).

[8] B. W. Dong, J. Cramer, K. Ganzhorn, H. Y. Yuan, E. J. Guo, S. T. B. Goennenwein, and M. Klaui, Spin Hall magnetoresistance in the non-collinear ferrimagnet GdIG close to the compensation temperature, J. Phys.: Condens. Matter **30**, 035802 (2018).

[9] M. U. Fayaz, M. S. Saleem, M. Gu, X. Zhou, F. Pan, and C. Song, Simultaneous detection of the spin Hall magnetoresistance and Joule heating-induced spin Seebeck EFfect in $Gd_3Fe_5O_{12}$/Pt bilayers, J. Appl. Phys. **126**, 183901 (2019).

[10] A. Quindeau, C. O. Avci, W. Liu, C. Sun, M. Mann, A. S. Tang, M. C. Onbasli, D. Bono, P. M. Voyles, Y. Xu, J. Robinson, G. S. D. Beach, and C. A. Ross, $Tm_3Fe_5O_{12}$/Pt heterostructures with perpendicular magnetic anisotropy for spintronic applications, Adv. Electron. Mater. **3**, 1600376 (2017).

[11] J. J. Bauer, E. R. Rosenberg, S. Kundu, K. A. Mkhoyan, P. Quarterman, A. J. Grutter, B. J. Kirby, J. A. Borchers, and C. A. Ross, Dysprosium iron garnet thin films with perpendicular magnetic anisotropy on silicon, Adv. Electron. Mater. **6**, 1900820 (2020).

[12] S. M. Zanjani and M. C. Onbaşlı, Predicting new iron garnet thin films with perpendicular magnetic anisotropy, J. Magn. Magn. Mater. **499**, 166108 (2020).

[13] Y. K. Liu, H. F. Wong, K. K. Lam, K. H. Chan, C. L. Mak, and C. W. Leung, Anomalous Hall effect in $Pt/Tb_3Fe_5O_{12}$ heterostructure: Effect of compensation point, J. Magn. Magn. Mater. **468**, 235 (2018).

[14] Q. Shao, A. Grutter, Y. Liu, G. Yu, C. Y. Yang, D. A. Gilbert, E. Arenholz, P. Shafer, X. Che, C. Tang, M. Aldosary, A. Navabi, Q. L. He, B. J. Kirby, J. Shi, and K. L. Wang, Exploring interfacial exchange coupling and sublattice effect in heavy metal/ferrimagnetic insulator heterostructures using Hall

measurements, x-ray magnetic circular dichroism, and neutron reflectometry, Phys. Rev. B **99**, 104401 (2019).

[15] J. J. Bauer, P. Quarterman, A. J. Grutter, B. Khurana, S. Kundu, K. A. Mkhoyan, J. A. Borchers, and C. A. Ross, Magnetic proximity effect in magnetic-insulator/heavy-metal heterostructures across the compensation temperature, Phys. Rev. B **104**, 094403 (2021).

[16] S. Y. Huang, H. L. Li, C. W. Chong, Y. Y. Chang, M. K. Lee, and J. C. A. Huang, Interface-induced spin Hall magnetoresistance enhancement in Pt-based tri-layer structure, Sci. Rep. **8**, 108 (2018).

[17] W. Amamou, I. V. Pinchuk, A. H. Trout, R. E. A. Williams, N. Antolin, A. Goad, D. J. O'Hara, A. S. Ahmed, W. Windl, D. W. McComb, and R. K. Kawakami, Magnetic proximity effect in Pt/CoFe$_2$O$_4$ bilayers, Phys. Rev. Mater. **2**, 011401(R) (2018).

[18] Y. M. Lu, Y. Choi, C. M. Ortega, X. M. Cheng, J. W. Cai, S. Y. Huang, L. Sun, and C. L. Chien, Pt magnetic polarization on Y$_3$Fe$_5$O$_{12}$ and magnetotransport characteristics, Phys. Rev. Lett. **110**, 147207 (2013).

[19] S. Geprägs, S. Meyer, S. Altmannshofer, M. Opel, F. Wilhelm, A. Rogalev, R. Gross, and S. T. B. Goennenwein, Investigation of induced Pt magnetic polarization in Pt/Y$_3$Fe$_5$O$_{12}$ bilayers, Appl. Phys. Lett. **101**, 262407 (2012).

[20] E. L. Jakubisova, S. Visnovsky, H. Chang, and M. Wu, Interface effects in nanometer-thick yttrium iron garnet films studied by magneto-optical spectroscopy, Appl. Phys. Lett. **108**, 082403 (2016).

[21] A. Mitra, O. Cespedes, Q. Ramasse, M. Ali, S. Marmion, M. Ward, R. M. D. Brydson, C. J. Kinane, J. F. K. Cooper, S. Langridge, and B. J. Hickey, Interfacial origin of the magnetisation suppression of thin film yttrium iron garnet, Sci. Rep. **7**, 11774 (2017).

[22] M. J. Roos, P. Quarterman, J. Ding, M. Wu, B. J. Kirby, and B. L. Zink, Magnetization and antiferromagnetic coupling of the interface between a 20 nm Y$_3$Fe$_5$O$_{12}$ film and Gd$_3$Ga$_5$O$_{12}$ substrate, Phys. Rev. Mater. **6**, 034401 (2022).

[23] Y. C. Chang, X. Li, R. D. Desautels, K. W. Lin, J. van Lierop, A. Ruotolo, and P. W. T. Pong, Influence of Cr$_2$O$_3$ thickness on the magnetic properties of NiFe/Cr$_2$O$_3$ bilayers deposited on SrTiO$_3$ single-crystalline substrate, Vacuum **140**, 126 (2017).

[24] T. Saerbeck, Polarization "down under": The polarized time-of-flight neutron reflectometer PLATYPUS, Rev. Sci. Instrum. **83**, 081301 (2012).

[25] See Supplemental Material at http://link.aps.org/supplemental/10.1103/PhysRevMaterials.7.124407 for the full details of the slit/instrument settings and reduction and fitting scripts of PNR and MCMC shown in Fig. 6, Fig. 7, Fig. 8, Fig. 9, and Fig. 10. Fig. 6 and Fig. 7 show the data of neutron reflectivity and SA and their fits at 300 K and 7 K; Fig. 8 shows the PNR data fitted to a SLD profile to quantify the layer magnetization; Fig. 9 and Fig. 10 show the correlation and uncertainty between the fitting parameters in a corner plot at 300 K and 7 K..

[26] J. A. Kaduk, S. J. L. Billinge, R. E. Dinnebier, N. Henderson, I. Madsen, R. Černý, M. Leoni, L. Lutterotti, S. Thakral, and D. Chateigner, Powder diffraction, Nat. Rev. Methods Primers **1**, 77 (2021).

[27] S. J. Callori, T. Saerbeck, D. L. Cortie, and K. W. Lin, Using polarized neutron reflectometry to resolve effects of light elements and ion exposure on magnetization, in *Solid State Physics*, edited by R. L. Stamps (Academic Press, United States, 2020), pp. 73–116.

[28] https://www-llb.cea.fr/prism/programs/simulreflec/simulreflec.html.

[29] A. R. J. Nelson and S. W. Prescott, refnx: Neutron and x-ray reflectometry analysis in Python, J. Appl. Crystallogr. **52**, 193 (2019).

[30] S. J. Pennycook, B. Rafferty, and P. D. Nellist, *Z*-contrast imaging in an aberration-corrected scanning transmission electron microscope, Microsc. Microanal. **6**, 343 (2000).

[31] K. Momma and F. Izumi, VESTA 3 for three-dimensional visualization of crystal, volumetric and morphology data, J. Appl. Crystallogr. **44**, 1272 (2011).

[32] K. I. Gnanasekar, P. Selvam, H. V. Keer, R. Pinto, S. C. Purandare, A. S. Tamhane, L. C. Gupta, and R. Vijayaraghavan, Superconductivity and valence state of Tb in Lu$_{1-x}$Tb$_x$Ba$_2$Cu$_3$O$_{7-\delta}$ ($0 \leqslant x \leqslant 0.7$), Appl. Phys. Lett. **65**, 1296 (1994).

[33] M. Xu and F. Zaera, Mechanistic studies of the thermal decomposition of metal carbonyls on Ni(100) surfaces in connection with chemical vapor deposition processes, J. Vac. Sci. Technol. **14**, 415 (1996).

[34] Q. H. Wu, M. Liu, and W. Jaegermann, X-ray photoelectron spectroscopy of La$_{0.5}$Sr$_{0.5}$MnO$_3$, Mater. Lett. **59**, 1980 (2005).

[35] V. Hasannaeimi and S. Mukherjee, Noble-metal based metallic glasses as highly catalytic materials for hydrogen oxidation reaction in fuel cells, Sci. Rep. **9**, 12136 (2019).

[36] J. M. Liang, X. W. Zhao, Y. K. Liu, P. G. Li, S. M. Ng, H. F. Wong, W. F. Cheng, Y. Z., J. Y. Dai, C. L. Mak, and C. W. Leung, The thickness effect on the compensation temperature of rare-earth garnet thin films, Appl. Phys. Lett. **122**, 242401 (2023).

[37] T. Nakatsuma, Bayesian analysis of ARMA-GARCH models: A Markov chain sampling approach, J. Econom. **95**, 57 (2000).

[38] A. R. McCluskey, A. J. Caruana, C. J. Kinane, A. J. Armstrong, T. Arnold, J. F. K. Cooper, D. L. Cortie, A. V. Hughes, J.-F. Moulin, A. R. J. Nelson, W. Potrzebowski, and V. Starostin, Advice on describing Bayesian analysis of neutron and x-ray reflectometry, J. Appl. Crystallogr. **56**, 12 (2023).

[39] M. R. Fitzsimmons and C. F. Majkrzak, Application of polarized neutron reflectometry to studies of artificially structured magnetic materials, in *Modern Techniques for Characterizing Magnetic Materials*, edited by Y. Zhu (Springer, New York, 2005), pp. 107–155.